

Tunable color display and efficient thermal regulation with grating colored radiative cooler

Chunzhen Fan(范春珍), Cong Ren(任聪), and Hengli Xie(谢恒立)

Citation: Chin. Phys. B, 2026, 35 (**6**): 064208. DOI: 10.1088/1674-1056/ae266f
http://cpb.iphy.ac.cn; http://iopscience.iop.org/cpb

What follows is a list of articles you may be interested in

Dual-wavelength polarization-tunable holographic response in an azobenzene-containing film

Hong Chen(陈红), Pan Wang(王潘), Ziyao Lyu(吕子瑶), and Changshun Wang(王长顺)
Chin. Phys. B, 2026, 35 (**5**): 054206. DOI: 10.1088/1674-1056/ae0b39

Simultaneous frequency stabilization of two 1550-nm lasers at single-photon level

Bo Yu(于波), Zhenqiang Yin(银振强), Weijie Ding(丁伟杰), Hui Yang(杨慧), and Weixin Liu(刘伟新)
Chin. Phys. B, 2026, 35 (**4**): 044208. DOI: 10.1088/1674-1056/ade072

Supersymmetry-driven segmented tapered laser for stabilized single transverse and longitudinal mode engineering

Yiwen Lou(楼亦文), Tian Lan(兰天), Jun Qi(齐军), Jinlong Zhao(赵金龙), Ying Li(李颖), Baiyi Qin(覃柏颐), Yuying Liu(刘豫颖), Xuesheng Liu(刘学胜), and Zhiyong Wang (王智勇)
Chin. Phys. B, 2026, 35 (**4**): 044207. DOI: 10.1088/1674-1056/ae29f9

Continuous three-dimensional varifocal of vortex beams with twisted metasurfaces

Yiyi Li(黎仪艺), Wangzhe Zhou(周王哲), Shaoqi Li(李少奇), Xiaoyan Huang(黄晓艳), Fen Zhao(赵芬), Man Yuan(袁满), Jiagui Wu(吴加贵), Huan Chen(陈欢), Zhaojian Zhang(张兆健), and Junbo Yang (杨俊波)
Chin. Phys. B, 2026, 35 (**3**): 034208. DOI: 10.1088/1674-1056/adfc42

Synchronized dual-wavelength mode-locked laser in normal dispersion regime

Yangrui Shi(史洋瑞), Haojing Zhang(张皓景), Yuxuan Ren(任俞宣), Junsong Peng(彭俊松), and Heping Zeng(曾和平)
Chin. Phys. B, 2025, 34 (**9**): 094207. DOI: 10.1088/1674-1056/add4fe

---

Tunable color display and efficient thermal regulation with grating colored radiative cooler

Chunzhen Fan(范春珍)†, Cong Ren(任聪), and Hengli Xie(谢恒立)

Key Laboratory of Materials Physics of Ministry of Education, School of Physics, Zhengzhou University, Zhengzhou 450001, *China*

(Received 2 September 2025; revised manuscript received 29 October 2025; accepted manuscript online 2 December 2025)

Integrating color display with radiative cooling is of great importance for applications in both aesthetic appeal and thermal management. However, current colored radiative coolers primarily rely on geometric modulation, resulting in monochromatic color and limiting their applicability. Here, we present a tunable colored radiative cooler (GCRC) comprising an upper grating emitter and a lower grating reflector. The emitter achieves a high average emissivity of 98.8% and 86.5% within the first and second atmospheric transparency windows simultaneously, and it demonstrates angular-insensitive emissivity ($> 70\%$) across 0–90° incident angle. Meanwhile, the grating reflector enables dynamic color manipulation through variations in polarization angle, dielectric layer thickness, and grating filling fraction. Notably, the GCRC demonstrates a maximum net nighttime cooling power of 232.08 $\mathrm{W\cdot m^{-2}}$ at 300 K, and it reaches up to 74.6 $\mathrm{W\cdot m^{-2}}$ under solar irradiation. Thus, our design not only delivers vibrant, adjustable color but also outperforms conventional radiative coolers in terms of cooling efficiency, making it a promising solution for architectural coatings, smart aesthetics, and advanced thermal management systems.

Keywords: grating, radiative cooling, color display, emitter, reflector

PACS: 42.25.Ja, 78.67.Pt, 44.40.+a

DOI: 10.1088/1674-1056/ae266f **CSTR:** 32038.14.CPB.ae266f

1. Introduction

Global warming imposes an urgent need to develop high-efficiency cooling technologies.[1,2] However, traditional cooling methods inevitably require the consumption of fossil energy, further exacerbating global warming.[3–5] This paradox underscores the demand for innovative, eco-friendly, and high-efficiency cooling solutions. Radiative cooling (RC) is considered an environmentally friendly cooling technology that emits heat into cold outer space through atmospheric transparency windows without consuming external energy.[6–9] The concept of RC was first introduced by Catalanotti *et al.*[3] in 1975 to reduce environmental temperature through selective emission. Since then, RC has demonstrated potential applications in roofs and windows of buildings,[10] personal thermal comfort,[11] solar photovoltaics,[12] thermal dissipation of electronic devices,[13] and even ice-melt reduction.[14] Traditional designs of radiative coolers primarily focus on optimizing cooling efficiency while maintaining high solar reflectance across the ultraviolet-to-infrared spectral range. In recent years, radiative cooling has evolved beyond simple cooling functions to encompass more complex integrations. For example, Qin *et al.*[15] established an electro-thermal model to evaluate the cooling effect on solar-cell performance. Chen *et al.*[16] designed and demonstrated a passive water-harvesting device that integrates hybrid directional solar heating with radiative cooling to achieve highly efficient water collection. To address more complex thermal challenges, Qin *et al.*[17] designed a thermally conductive radiative-cooling film with a porous structure for dissipating local hot spots in outdoor flexible electronics. For large-scale applications, Liu *et al.*[18] developed a thin and durable radiative cooling paint by incorporating hexagonal boron nitride platelets, achieving highly efficient passive daytime radiative cooling. Driven by these pioneering works, advanced radiative-cooling technologies are increasingly being developed as multifunctional, durable, and system-integrated solutions. To achieve this, radiative coolers typically maximize solar-radiation reflection and therefore exhibit a white appearance.[19–21] However, practical applications often require specific colors to fulfill multifaceted functional needs, including aesthetic integration, environmental concealment, and adaptive thermoregulation,[22] which necessitates selective reflection or absorption of visible light.[23–25]

Colored radiative coolers (CRCs) facilitate the simultaneous realization of aesthetic color presentation and passive thermal regulation. Conventionally, achieving desired colors has predominantly relied on pigments or dyes.[26–28] To reconcile coloration with RC performance, selective narrow-band visible-light absorption becomes critical. To date, the design of CRCs has mainly utilized plasmonic resonance,[29] Fabry–Pérot cavities,[30–32] Mie scattering,[33] photonic crystals,[34,35] and iridescent periodic interference structures.[36–40] For instance, Li *et al.*[41] pioneered this concept through constructive interference in multilayer emitters to achieve photonic thermal management. Zhu *et al.*[42] incor-

†Corresponding author. E-mail: chunzhen@zzu.edu.cn

© 2026 Chinese Physical Society and IOP Publishing Ltd. All rights, including for text and data mining, AI training, and similar technologies, are reserved.

porated transparent quartz bars with high mid-IR emissivity onto the surface, reducing temperatures even under significant non-radiative heat-exchange conditions. Chen *et al.*[26] developed a color-tunable bilayer coating, in which the top layer selectively absorbed specific wavelengths of visible light to produce color, while the bottom layer reflected near-infrared radiation to enable efficient RC with vivid coloration. Furthermore, nanoparticle-based inks were fabricated into colorful daytime RC films via inkjet printing. By incorporating quantum dots for spectral conversion, these white films achieved a temperature reduction of up to 6.12 °C below ambient.[43] Cai *et al.*[44] employed inorganic nanoparticles as colorants for scalable colored and infrared-transparent fabrics. Wang *et al.*[45] developed metal–insulator–metal and multilayer structures to achieve a light pink RC device. Structural color originates from the interaction of light with precisely engineered micro/nanostructures and offers superior stability. Despite significant progress in achieving vibrant, long-lasting colors with structural CRCs, they generally face two key challenges: limited dynamic color tunability and angular dependence. For example, Shi *et al.*[46] utilized a complex multilayer structure to achieve a broad static color gamut and a 5.8 °C temperature reduction, while Yuan *et al.*[47] demonstrated precise thermal-load control for a fixed pink color. Although Ding *et al.*[48] enabled sub-ambient cooling even for dark colors, the colors in these designs are dictated by fixed nanostructures and cannot be altered after fabrication. Furthermore, many structural-color approaches exhibit iridescence, where the color shifts with viewing angle, limiting their use in applications requiring a stable appearance. Despite significant progress, structural-color CRCs still face the challenge that their colors are determined by fixed nanostructures,[46–48] thereby limiting applications that require dynamic control. Multifunctional radiative coolers continue to advance,[49] but most studies focus on color preservation rather than active color tuning. Therefore, achieving a CRC that simultaneously delivers efficient cooling, high durability, angularly stable coloration, and dynamic tunability remains a key objective, which motivates the present study.

In this study, we present a novel design of a grating-colored radiative cooler (GCRC). Specifically, a Si_3N_4 triangular-prism grating on a SiO_2 layer constitutes the top emitter, achieving average emissivities of 98.8% and 86.5% within the first and second atmospheric transparency windows, respectively. The bottom reflector consists of an Al prism grating deposited on Ag and SiO_2 layers. To achieve an aesthetic color display, the color can be flexibly adjusted by controlling the polarization angle, the filling fraction of the prism grating, and the thickness of the intermediate dielectric layer. To evaluate the cooling performance, the radiative-cooling power and absorbed solar energy are calculated as functions of temperature while considering different convection coefficients and incident angles. Furthermore, the tunable RGB characteristics and power-loss ratio are investigated to demonstrate the tunable color display and cooling performance. Therefore, this study provides valuable guidance for efficient radiative heat dissipation and vivid color display.

2. Design and theory

2.1. Structure design

The overall design of the GCRC is illustrated in Fig. 1(a). The top emitter consists of a Si_3N_4 triangular grating on a SiO_2 layer, which is responsible for high emissivity within the atmospheric transparency windows. The bottom reflector consists of an Al prismatic grating on a SiO_2/Ag multilayer. The color display is determined by the reflector, where interference within the multilayer can be precisely tuned by the thickness of the SiO_2 layer, the grating filling fraction, and the polarization angle. The constituent materials Si_3N_4 and SiO_2, which possess intrinsic absorption, were chosen. Their strong inherent absorption occurs in the mid-infrared region and originates from phonon vibrational modes in the crystal lattice. Specifically, Si_3N_4 exhibits high absorption at 10.9 μm, whereas SiO_2 absorbs around 9.27 μm. Figure 1(b) illustrates the side view of the GCRC, where the width of the top grating (a_1) is 3 μm and its periodicity (Λ_1) is 7 μm. For the bottom grating, the width and period are $a_2 = 30$ nm and $\Lambda_2 = 300$ nm, respectively. The thicknesses of the GCRC from top to bottom are $d_1 = 8$ μm, $d_2 = 9$ μm, $d_3 = 50$ nm, $d_4 = 65$ nm, and $d_5 = 200$ nm. These structural parameters were determined through a systematic optimization process based on finite-element methods using COMSOL Multiphysics. The detailed optimization of the geometric parameters is provided in the Supporting Information (Fig. S3). In addition, the filling fraction of the grating is defined as the width divided by the period. The optical constants of Ag, SiO_2, Al, and Si_3N_4 were taken from Ref. [50]. To obtain the optical properties of the GCRC, numerical simulations were carried out using COMSOL Multiphysics. A three-dimensional simulation domain was first established with the incident plane wave propagating along the z-axis. Periodic boundary conditions were applied along the x and y directions to simplify the model. A perfectly matched layer was applied in the z direction to prevent unphysical reflections at the boundaries. Finally, a finite element solution was obtained using a free tetrahedral and triangular mesh grid. Furthermore, the designed photonic metamaterial can be realized experimentally with recent advancements in nanofabrication techniques. First, uniform Ag/SiO_2/Al thin films are deposited layer by layer via direct current (DC) magnetron sputtering.[51,52] Subsequently, the Al prism grating is created using photolithography and inductively coupled plasma reactive ion etching.[53,54] Chemical spin-coating is employed to

uniformly apply PDMS onto the prism grating. SiO_2/Si_3N_4 thin films are then deposited using DC magnetron sputtering. Finally, a sacrificial layer is coated on the top, and the grating structure is obtained through photolithography and wet-etching processes.[55,56] A detailed fabrication procedure with a process flowchart is provided in the Supporting Information (Fig. S4).

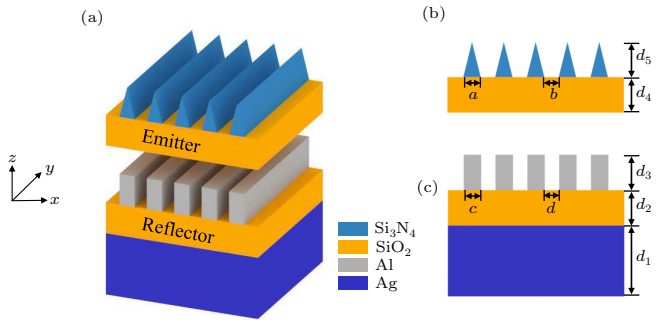


Fig. 1. (a) Schematic view of the GCRC, (b) *xoz*-plane view of the GCRC. Parameters: $a_1 = 3$ μm, $\Lambda_1 = 7$ μm, $a_2 = 30$ nm, $\Lambda_2 = 300$ nm, $d_1 = 8$ μm, $d_2 = 9$ μm, $d_3 = 50$ nm, $d_4 = 65$ nm, $d_5 = 200$ nm.

2.2. Radiative cooling power

According to the law of energy conservation, the cooling performance of the designed GCRC can be evaluated via the net RC power, $P_{\text{cooling}}(T)$, which consists of four components as shown in Eq. 1. P_{rad} represents the output power of the cooler, P_{atm} denotes the power absorbed from the atmosphere per unit area, P_{sun} is the absorbed solar energy, and P_{loss} indicates parasitic heat loss. Their relationship can be expressed as

$$P_{\text{cooling}}(T) = P_{\text{rad}}(T) - P_{\text{atm}}(T_{\text{amb}}) - P_{\text{sun}} - P_{\text{loss}}(T), \quad (1)$$

where T and T_{amb} are the temperatures of the cooler and the ambient, respectively. The output cooling power from the emitter is given by

$$\begin{aligned} P_{\text{rad}}(T) &= \int\int_0^{\infty} I_{\text{BB}}(T,\lambda)\,\varepsilon(\lambda,\theta)\,\mathrm{d}\lambda\,\mathrm{d}\Omega, \\ I_{\text{BB}}(T,\lambda) &= \frac{2hc^2}{\lambda^5}\frac{1}{\exp\left(\dfrac{hc}{\lambda k_{\text{B}} T}\right)-1}, \end{aligned} \quad (2)$$

where λ is the wavelength of the incident electromagnetic wave, $\varepsilon(\lambda,\theta)$ is the spectral and directional absorptivity, and $\int \mathrm{d}\Omega$ denotes the integral over all solid angles. Here, h is Planck's constant, k_{B} is Boltzmann's constant, and c is the speed of light.[57]

The atmospheric thermal radiative power, P_{atm}, is expressed as

$$\begin{aligned} P_{\text{atm}}(T_{\text{amb}}) &= 2\pi \int_0^{\pi/2} \sin\theta\cos\theta\,\mathrm{d}\theta \\ &\times \int_0^{\infty} I_{\text{BB}}(T_{\text{amb}},\lambda)\,\varepsilon(\lambda,\theta)\,\varepsilon_{\text{atm}}(\lambda,\theta)\,\mathrm{d}\lambda. \end{aligned} \quad (3)$$

The atmospheric emissivity is defined as

$$\varepsilon_{\text{atm}}(\lambda,\theta) = 1 - [\tau(\lambda)]^{1/\cos\theta}, \quad (4)$$

where $\tau(\lambda)$ is the atmospheric transmittance in the zenith direction.[58,59]

The solar energy absorbed by the radiative cooler, P_{sun}, is

$$P_{\text{sun}} = \int_0^{\infty} \varepsilon(\lambda)\, I_{\text{AM1.5}}(\lambda)\,\mathrm{d}\lambda, \quad (5)$$

where $I_{\text{AM1.5}}(\lambda)$ is the solar spectral irradiance under the AM1.5 standard atmosphere. Here, it is taken as 1000 $\text{W}\cdot\text{m}^{-2}$.[60]

The parasitic heat loss is given by

$$P_{\text{loss}}(T) = h_{\text{c}}(T_{\text{amb}} - T), \quad (6)$$

where h_{c} is the non-radiative heat transfer coefficient.[61]

2.3. Color display

Color display is primarily influenced by the spectral power distribution (SPD) of the incident light source, the reflectance of the object across the visible spectrum, and the color matching functions. In this study, the standard illuminant D65 was selected as the reference light source. The reflectance and corresponding color matching functions are significantly influenced by both the composition and configuration of the target object. Color matching functions quantify the responses of the human visual system to different wavelengths, with the CIE 1931 standard colorimetric system providing a widely accepted theoretical framework for optical and colorimetric analyses.[62] This framework enables the derivation of chromaticity coordinates (x,y,z) through integration of the standard color matching functions with the SPD. The tristimulus values (X,Y,Z) are calculated as

$$\begin{pmatrix} X \\ Y \\ Z \end{pmatrix} = k \int_0^{\infty} I(\lambda) R(\lambda) \begin{pmatrix} \bar{x}(\lambda) \\ \bar{y}(\lambda) \\ \bar{z}(\lambda) \end{pmatrix} \mathrm{d}\lambda, \quad (7)$$

where $I(\lambda)$ represents the spectral power distribution of the incident light source, $R(\lambda)$ is the spectral reflectance of the object, and $\bar{x}(\lambda)$, $\bar{y}(\lambda)$, $\bar{z}(\lambda)$ are the standard CIE color matching functions. A normalization constant k ensures that Y corresponds to the reference light intensity, and it is defined as

$$k = \frac{100}{\int_0^{\infty} I(\lambda)\bar{y}(\lambda)\,\mathrm{d}\lambda}. \quad (8)$$

The chromaticity coordinates are obtained by normalizing the tristimulus values

$$(x,y,z) = \left(\frac{X}{X+Y+Z}, \frac{Y}{X+Y+Z}, \frac{Z}{X+Y+Z}\right). \quad (9)$$

Based on the tristimulus values (X, Y, Z), the RGB values are obtained using the following transformation matrix

$$\begin{pmatrix} R \\ G \\ B \end{pmatrix} = \begin{pmatrix} 0.41847 & -0.15866 & -0.082835 \\ -0.091169 & 0.25243 & 0.015708 \\ 0.00092090 & -0.0025498 & 0.17860 \end{pmatrix} \begin{pmatrix} X \\ Y \\ Z \end{pmatrix}. \tag{10}$$

Finally, the color display can be predicted by calculating the RGB values.

3. Results and discussion

Figure 2(a) presents the reflectance of the designed GCRC in the visible band under TM and TE polarizations. It is clearly observed that the resonance dip occurs at 470 nm for the TM mode and at 581 nm for the TE mode, demonstrating polarization-dependent behavior. Figure 2(b) illustrates the electric field distributions at 470 nm and 581 nm, respectively. The field is primarily concentrated on both sides of the silver layer at 470 nm, indicating a strong dipole resonance. A redshift in the absorption dip leads to a color transition from orange to purple, with the electric field mainly concentrated in the middle region of the SiO_2 layer.[63] To achieve high emissivity, Si_3N_4 and SiO_2 are selected for their intrinsically high absorption in the atmospheric transparency windows. Figure 2(c) illustrates the emissivity of the designed emitter within the atmospheric transparency windows. The high average emissivity results in strong emission in both TM and TE polarizations, as provided in the Supporting Information (Fig. S2). The atmospheric transmission spectra, shaded in blue, utilize standard ATRAN model data, representing typical clear-sky conditions at high-altitude and arid observatory sites.[64] The emitter demonstrates a broad and high emissivity profile across the atmospheric transparency windows. The average emissivity within the first and second atmospheric transparency windows reaches high values of 0.988 and 0.865, which are desirable for enhanced heat dissipation. The patterned unit cell of the emitter acts as a resonator and excites size-dependent dielectric resonances. These resonances effectively confine infrared light within the Si_3N_4 grating, increasing photon–material interactions and substantially improving absorption efficiency within the atmospheric transparency band.

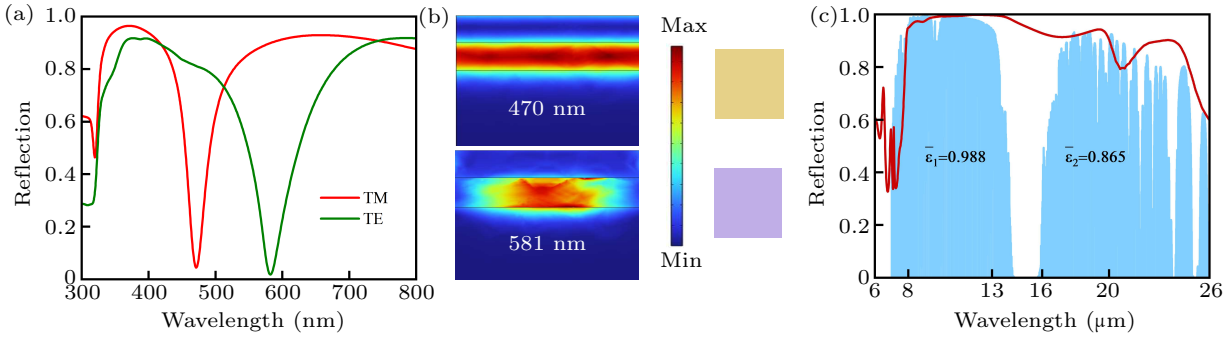


Fig. 2. (a) Reflection spectra of the GCRC in the visible band, (b) electric-field distributions and corresponding color displays in the *yoz* plane at 470 nm and 581 nm, respectively, (c) emissivity of the GCRC within the atmospheric transparency windows.

To systematically investigate the tunable color display, we calculated the reflection as a function of thickness (d_4) in Fig. 3(a). Under TM polarization, the resonance dip shifts from 435 nm to 504 nm as d_4 increases from 55 nm to 75 nm, indicating a redshift. The corresponding CIE 1931 chromaticity diagram is shown in Fig. 3(b). The points move from position 1 to 5, with the color shifting from pink to yellow. Similarly, Fig. 3(c) presents the reflection under TE polarization, where the resonance dip redshifts from 570 nm to 588 nm as the dielectric thickness increases. Meanwhile, the chromaticity coordinates move from position 1 to 5 on the CIE 1931 diagram, with the observed color transitioning from purple to light green. These results demonstrate that a wide range of vivid colors can be achieved in the GCRC by simply tuning the thickness of the intermediate dielectric layer, resulting from modulated optical path lengths that alter the interference conditions. The tunable color originates from a Fabry–Pérot resonance within the cavity formed by the bottom Ag mirror and the top Al grating. Strong resonance occurs when the incident light is trapped in the cavity through constructive interference, leading to a strong absorption dip in the reflection. For a fixed incident angle, the resonant wavelength is directly proportional to the thickness of the SiO_2 layer. Therefore, increasing the thickness of the SiO_2 layer increases the optical path, causing a redshift of the resonant absorption peak.[65,66]

The tunable color display is also explored by varying the filling fraction (f) of the prismatic grating. Figure 4(a) shows the reflectance under TM polarization as f increases from 5% to 25%. Here, the thickness of the intermediate dielectric layer is fixed at 65 nm. The corresponding resonant dip exhibits a blueshift, shifting from 508 nm to 453 nm. The relevant points on the CIE 1931 chromaticity diagram rotate counterclockwise in Fig. 4(b), indicating a color transition from pink to yellow. The corresponding analysis for TE polarization is provided in the Supporting Information (Fig. S5), which also demonstrates color variation with different filling frac-

tions. The designed grating structure induces strong diffraction and interference in the visible band, enabling selective wavelengths of light to couple with guided modes and generate pronounced resonance dips to manifest structural colors. By modulating the filling fraction, the proportion of high-refractive-index regions within each period is altered, thereby tuning the dispersion characteristics of the guided modes. Thus, a redshift of the resonance position occurs with a larger filling fraction, which is consistent with Refs. [67–69].

Figure 5 comprehensively illustrates the tunable color display through variations in the intermediate dielectric layer thickness, grating filling fraction, and polarization mode under TM and TE polarization. In the TM mode, the colors predominantly fall within the orange spectrum in Fig. 5(a), while under TE mode, the colors are concentrated within the blue region of the chromaticity space in Fig. 5(b). The vivid color spectrum indicates a strong polarization-tunable property, making the GCRC well-suited for information encryption and color coding.

Figure 6 presents the angular-dependent emissivity of the GCRC. For both TM and TE polarizations, the average emissivity decreases with increasing incident angle, and the overall emissivity in the first atmospheric transparency window is higher than that in the second window. Owing to the asymmetric triangular prism grating structure, the average emissivity in the first atmospheric transparency window under TM polarization is higher than that under TE polarization. It is also found that the average emissivity remains above 0.7 in both the first and second atmospheric transparency windows.

The high and angle-insensitive emissivity of the emitter is attributed to the synergy between the intrinsic absorption of the constituent materials and the patterned grating. First, the selected materials, Si_3N_4 and SiO_2, inherently possess strong dielectric absorption in the mid-infrared atmospheric windows. Second, the designed micrometer-scale prismatic grating structure effectively increases the interaction path length for thermal radiation within these absorptive materials through diffraction and scattering effects. These results indicate that the prismatic grating emitter maintains high emissivity even under varying solar positions, making it well-suited for continuous radiative cooling in practical applications.

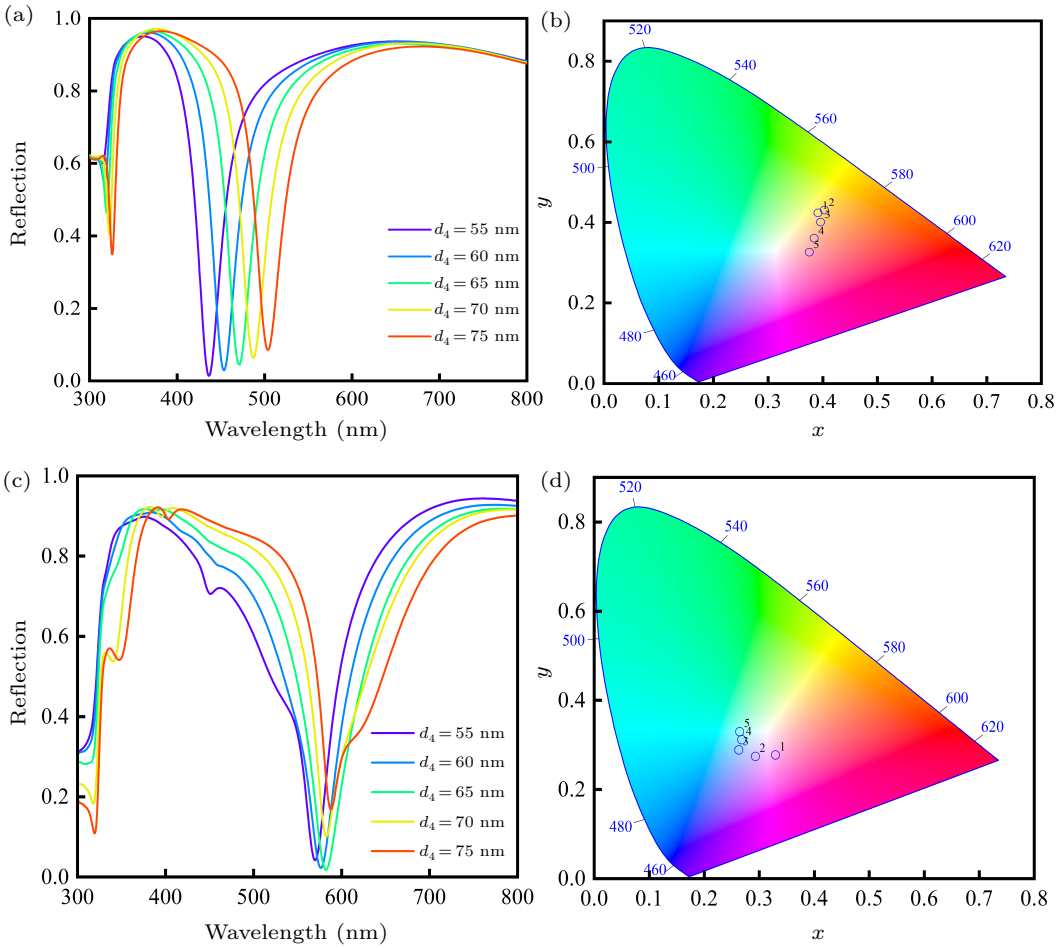


Fig. 3. Tunable color display with different thicknesses of the dielectric layer. (a) Reflection spectra as a function of d_4 under TM polarization, (b) corresponding color points on the CIE 1931 chromaticity diagram under TM polarization, (c) reflection spectra as a function of d_4 under TE polarization, (d) corresponding color points on the CIE 1931 chromaticity diagram under TE polarization.

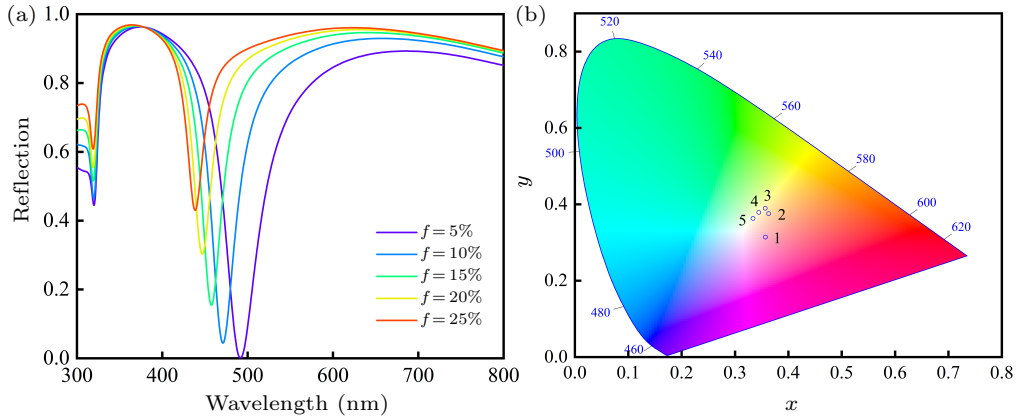


Fig. 4. Tunable color display with varying filling fraction of the prismatic grating. (a) Reflection spectra of the GCRC under TM polarization as a function of the filling fraction, (b) corresponding color points on the CIE 1931 chromaticity diagram.

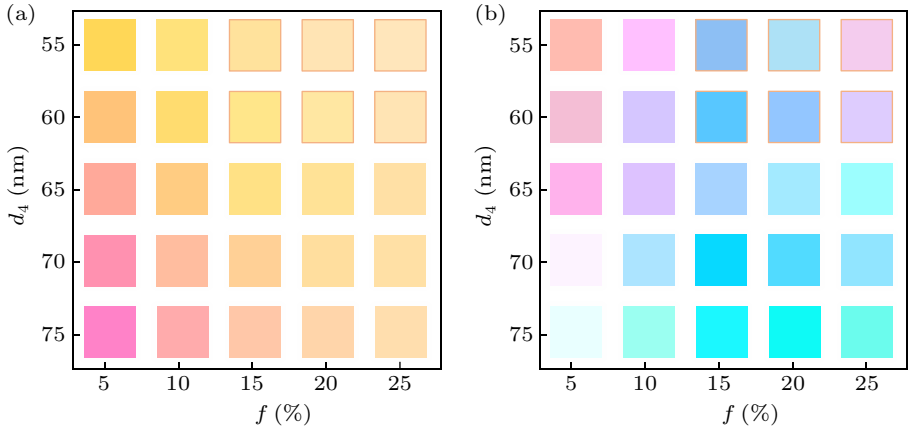


Fig. 5. Color display of the GCRC with varying filling fraction (f) and dielectric thickness (d_4), (a) TM polarization, (b) TE polarization.

To evaluate the cooling performance of the GCRC, we calculated the net cooling power as a function of temperature, assuming no heat transfer through conduction or convection ($h_c = 0$). The radiative power (P_{rad}), the net daytime cooling power ($P_{daytime}$), and the nighttime cooling power (P_{night}) are plotted in Fig. 7(a). The cooling power increases with temperature, and the differences between them remain constant, indicating approximately parallel trends. Notably, the net nighttime cooling power reaches 232.08 W·m^{-2} at 300 K, and the net daytime cooling power is 74.6 W·m^{-2}. The reduced daytime cooling performance is attributed to partial absorption of solar radiation in the visible range to maintain color display.

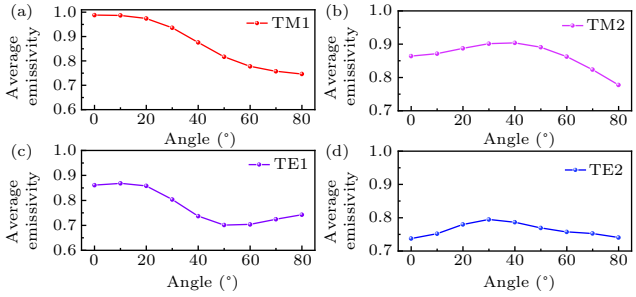


Fig. 6. Angular-dependent average emissivity of the GCRC in the first and second atmospheric transparency windows as a function of incident angle for TM and TE polarizations.

The influence of convective and conductive heat transfer is further considered in Fig. 7(b). With increasing h_c from 0 to 9 W·m^{-2}·K^{-1}, the equilibrium temperature of the cooler increases accordingly. Notably, the cooler achieves an equilibrium temperature of 294.2 K at $h_c = 9$ W·m^{-2}·K^{-1}, which is 5.8 K below the ambient temperature, underscoring the promising potential of the grating-based CRC for practical applications.

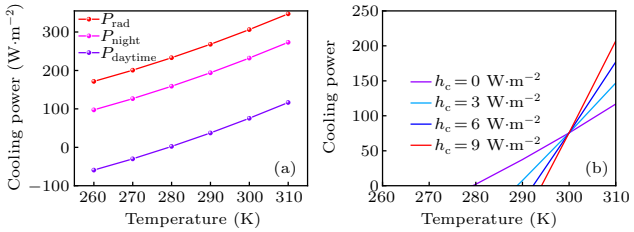


Fig. 7. (a) Net radiative cooling (RC) power, daytime RC power, and nighttime RC power of the GCRC as a function of temperature, (b) RC power under varying non-radiative heat transfer coefficients (h_c).

The relevant CRCs in terms of structure, color display, average emissivity ($\bar{\varepsilon}_{8-13\ \mu m}$), net cooling power ($P_{net}$), and temperature reduction (ΔT) are summarized in Table 1 (Supporting Information Fig. S1). Our GCRC exhibits a significantly higher cooling power of 232 W·m^{-2} at night and 74.6 W·m^{-2} during the day, surpassing many conventional colored radiative coolers.

To directly illustrate that our design not only achieves considerable RC performance but also displays vivid colors, Table 1 presents the varied RGB values and the corresponding thermal loss ratios for different thicknesses of the dielectric layer. Under TM polarization, the color display predominantly lies in the orange range. Analysis of the RGB values indicates that the red component (R) remains relatively stable, the green component (G) initially increases and then decreases, and the blue component (B) continuously increases, resulting in a color transition from yellow to reddish-orange.

It is worth noting that absorption in the visible spectrum slightly reduces the RC power; therefore, the thermal loss ratio is also calculated. It is defined as the ratio of solar absorption power to RC power, $\delta = P_{\text{sun}}/P_{\text{rad}}$. As the dielectric thickness increases, δ shows a slight variation of 2%, ranging from 44.2% to 46.2%.

As a direct application of our design, a conceptual diagram illustrating the color display with different polarization angles, grating filling fractions, and dielectric thicknesses is provided. These results confirm that the GCRC retains strong cooling capability while offering vivid colors. The relevant figure is provided in the Supporting Information (Fig. S6).

Table 1. Tunable RGB values and corresponding thermal loss ratios for different dielectric layer thicknesses.

d_2	55 nm	60 nm	65 nm	70 nm	75 nm
R	255	255	255	255	255
G	206	220	204	189	171
B	123	111	130	159	172
P_{loss}	42.2%	43.7%	44.6%	45.3%	46.2%

4. Conclusion

In summary, we have proposed a novel radiative cooler that exhibits dual functions of high cooling efficiency and versatile color display. The top emitter achieves high average emissivities of 98.8% and 86.5% within the first and second atmospheric transparency windows, respectively. Tunable and vivid colors can be achieved by varying the dielectric layer thickness, filling fraction, and polarization angle. The high emissivity persists even at large incident angles, which further confirms its excellent cooling performance. Based on calculations of RC power, solar absorption, and thermal loss ratio, it is found that the proposed design holds great potential for practical applications requiring both aesthetic color control and efficient thermal management. Therefore, this work provides valuable guidance for the development of devices that integrate visual appearance with effective cooling performance.

Acknowledgment

This work was supported by the Optoelectronic Information Detection and Application Engineering Research Center of Henan Province.

References

[1] Li X, Sun B, Sui C, Nandi A, Fang H, Peng Y, Tan G and Hsu P C 2020 *Nat. Commun.* **11** 6101
[2] Pérez-Lombard L, Ortiz J and Pout C 2008 *Energy Build.* **40** 394
[3] Broecker W S 1975 *Science* **189** 460
[4] Chen M, Pang D, Chen X, Yan H and Yang Y 2022 *EcoMat* **4** e12153
[5] Huang M C, Yang M, Guo X J, Xue C H, Wang H D, Ma C Q, Bai Z, Zhou X, Wang Z, Liu B Y, Wu Y G, Qiu C W, Hou C and Tao G 2023 *Prog. Mater. Sci.* **137** 101144
[6] Jia Y, Wang X, Yin H, Yao H, Wang J and Fan C 2021 *Appl. Opt.* **60** 5699
[7] Zhao D, Aili A, Yin X, Tan G and Yang R 2019 *Appl. Phys. Rev.* **6** 021306
[8] Catalanotti S, Cuomo V, Piro G, Ruggi D, Silvestrini V and Troise G 1975 *Sol. Energy* **17** 83
[9] Yin H and Fan C 2023 *Chin. Phys. Lett.* **40** 077801
[10] Mandal J, Yang Y, Yu N and Raman A P 2020 *Joule* **4** 1350
[11] Wu M, Shao Z, Zhao N, Zhang R, Yuan G, Tian L, Zhang Z, Gao W and Bai H 2023 *Science* **382** 1379
[12] Bao H, Yan C, Wang B, Fang X, Zhao C Y and Ruan X 2017 *Sol. Energy Mater. Sol. Cells* **168** 78
[13] Li J, Fu Y, Zhou J, Yao K, Ma X, Gao S, Wang Z, Dai J G, Lei D and Yu X 2023 *Sci. Adv.* **9** eadg1837
[14] Li J, Liang Y, Li W, Xu N, Zhu B, Wu Z, Wang X, Fan S, Wang M and Zhu J 2022 *Sci. Adv.* **8** eabj9756
[15] Ye Q, Chen X, Yan H and Chen M 2025 *Mater. Today Phys.* **50** 101626
[16] Liu S, Zhang F, Chen X, Yan H, Chen W and Chen M 2024 *J. Energy Chem.* **90** 176
[17] Ye Q, Yan H and Chen M 2025 *Appl. Phys. Lett.* **127** 103906
[18] Chen M, Wang J and Li Q 2025 *Adv. Funct. Mater.* **35** 2407761
[19] Kou J L, Jurado Z, Chen Z, Fan S and Minnich A J 2017 *ACS Photonics* **4** 626
[20] Gentle A R and Smith G B 2010 *Nano Lett.* **10** 373
[21] Fan C, Wu C L, Wang Y, Wang B and Wang J 2024 *Phys. Rep.* **1077** 1
[22] Han X and Fan C 2024 *Chin. Phys. B* **33** 442
[23] Wang L, Wang T, Yan R, Yue X, Wang H, Wang Y, Zhang J, Yuan X, Zeng J and Wang J 2023 *Nano Lett.* **23** 5581
[24] Xi W, Liu Y, Zhao W, Hu R and Luo X 2021 *Int. J. Therm. Sci.* **170** 107172
[25] Xie H, Yin H and Fan C 2024 *Chin. Phys. Lett.* **41** 044202
[26] Chen Y, Mandal J, Li W, Smith-Washington A, Tsai C C, Huang W, Shrestha S, Yu N, Han R P S, Cao A and Yang Y 2020 *Sci. Adv.* **6** eaaz5413
[27] Son S, Chae D, Lim H, Ha J, Park J, Ju S, Park J, Kim W and Lee H 2023 *Adv. Eng. Mater.* **25** 2201254
[28] Yin H and Fan C 2023 *Results Phys.* **45** 106216
[29] Pirouzfam N, Menguc M P and Sendur K 2023 *Sol. Energy Mater. Sol. Cells* **253** 112225.
[30] Peng Y, Lai J C, Xiao X, Jin W, Zhou J, Yang Y, Gao X, Tang J, Fan L, Fan S, Bao Z and Cui Y 2023 *Proc. Natl. Acad. Sci. USA* **120** e2300856120
[31] Chen M, Pang D and Yan H 2022 *Appl. Therm. Eng.* **216** 119125
[32] Lee G J, Kim Y J, Kim H M, Yoo Y J and Song Y M 2018 *Adv. Opt. Mater.* **6** 1800707
[33] Atvars A 2021 *J. Opt. Soc. Am. B* **38** 3116
[34] Fan C, Ren C, Xie H and Xia H 2025 *Phys. Scr.* **100** 085539
[35] Baek K, Kim Y, Mohd-Noor S and Hyun J K 2020 *ACS Appl. Mater. Interfaces* **12** 5300
[36] Zhao J, Li X, Zhong L and Chen G 2009 *J. Phys.: Conf. Ser.* **183** 012018
[37] Kim H H, Kwak S, Lee J, Im E, Raman A P and Lee S 2024 *Cell Rep. Phys. Sci.* **5** 102068
[38] Lin K T, Nian X, Li K, Han J, Zheng N, Lu X, Guo C, Lin H and Jia B 2023 *eLight* **3** 22
[39] Cho J W, Park S J, Park S J, Kim Y B, Moon Y J and Kim S K 2021 *Nano Lett.* **21** 3974
[40] Yao H, Wang X, Yin H, Jia Y, Gao Y, Wang J and Fan C 2021 *Chin. Phys. B* **30** 064214
[41] Su M, Wang X, Mu K and Fan C 2024 *Phys. Scr.* **99** 115545
[42] Li W, Shi Y, Chen Z and Fan S 2018 *Nat. Commun.* **9** 4240
[43] Zhu L, Raman A and Fan S 2013 *Appl. Phys. Lett.* **103** 223902

[44] Yoon T Y, Son S, Min S, Chae D, Woo H Y, Chae J Y, Lim H, Shin J, Paik T and Lee H 2021 *Mater. Today Phys.* **21** 100510
[45] Cai L, Peng Y, Xu J, Zhou C, Zhou C, Wu P, Lin D, Fan S and Cui Y 2019 *Joule* **3** 1478
[46] Xi W, Liu Y, Zhao W, Hu R and Luo X 2021 *Int. J. Therm. Sci.* **170** 107172
[47] Shi Y, Zhu A, Li Q and Fan D 2025 *Mater. Today Phys.* **55** 101759
[48] Yuan H, Yang C, Zheng X, Mu W, Wang Z, Yuan W, Zhang Y, Chen C, Liu X and Shen W 2018 *Opt. Express* **26** 27885
[49] Tang K, Dong K, Li J, Gordon M P, Reichertz F G, Kim H, Rho Y, Wang Q, Lin C Y, Grigoropoulos C P, Javey A, Urban J J, Yao J, Levinson R and Wu J 2021 *Science* **374** 1504
[50] Polyanskiy M N 2024 *Sci. Data* **11** 94
[51] Cunha N F, Al-Rjoub A, Rebouta L, Vieira L G and Lanceros-Mendez S 2020 *Thin Solid Films* **694** 137736
[52] Fukasawa T, Kubota K, Shindo H and Horiike Y 1994 *Jpn. J. Appl. Phys.* **33** 7042
[53] Cho J W, Lee T I, Kim D S, Park K H, Kim Y S and Kim S K 2018 *J. Opt.* **20** 09LT01
[54] Zhao Y, Liu H, Qin H, Chu X, Wang X, Wang X, Cai K, Liu D, Wang C and Wang J 2011 *Rare Met.* **30** 651
[55] Pouria R, Chow P K, Tiwald T, Zare S and Edalatpour S 2022 *Appl. Phys. Lett.* **121** 131702
[56] Kumar M D, Kim H and Kim J 2015 *Sol. Energy* **117** 180
[57] Raman A P, Anoma M A, Zhu L, Rephaeli E and Fan S 2014 *Nature* **515** 540
[58] Liu J, Zhang Y, Li S, Valenzuela C, Shi S, Jiang C, Wu S, Ye L, Wang L and Zhou Z 2023 *Chem. Eng. J.* **453** 139739
[59] Yin H, Yao H, Jia Y, Wang J and Fan C 2021 *J. Phys. D: Appl. Phys.* **54** 345501
[60] Han D, Ng B F and Wan M P 2020 *Sol. Energy Mater. Sol. Cells* **206** 110270
[61] Jayamaha S E G, Wijeysundera N E and Chou S K 1996 *Build. Environ.* **31** 399
[62] Sheng C, An Y, Du J and Li X 2019 *ACS Photonics* **6** 2545
[63] Shuvo M M K, Hossain M I, Mahmud S, Rahman S, Topu M T H, Hoque A, Islam S S, Soliman M S, Almalki S H A, Islam M S and Islam M T 2022 *Sci. Rep.* **12** 4857
[64] Tokunaga A T, Simons D A and Vacca W D 2002 *Publ. Astron. Soc. Pac.* **114** 180
[65] Wang T, Liu Y, Dong Y, Yin X, Lei D and Dai J G 2025 *Adv. Mater.* **37** 2414300
[66] Keawmuang H, Badloe T, Lee C, Park J and Rho J 2024 *Sol. Energy Mater. Sol. Cells* **271** 112848
[67] Kuang K, Wang Q, Yuan X, Yang Y, Chu H, Chang F and Peng W 2024 *J. Phys. D: Appl. Phys.* **57** 055106
[68] Koirala I, Shrestha V R, Park C S, Lee S S and Choi D Y 2017 *Sci. Rep.* **7** 40073
[69] Jeon J, Chun B S, Seo Y, Kim M, Kim H, Kim Y, Kim J S and Lee S J 2023 *Nanoscale Adv.* **5** 633